Journal of
**Synchrotron
Radiation**

ISSN 0909-0495

Received 22 September 2004
Accepted 4 January 2005

Troika II: a versatile beamline for the study of liquid and solid interfaces

Detlef-M. Smilgies,[a,b]* Nathalie Boudet,[c] Bernd Struth[b] and Oleg Konovalov[b]

[a]Cornell High Energy Synchrotron Source (CHESS), Wilson Laboratory, Cornell University, Ithaca, NY 14853, USA, [b]European Synchrotron Radiation Facility, 6 Rue Horovitz, BP 220, F-38043 Grenoble CEDEX, France, and [c]Laboratoire de Cristallographie, Centre National de la Recherche Scientifique (CNRS), BP 166, 38042 Grenoble CEDEX 09, France. E-mail: dms79@cornell.edu

The Troika II beamline at the European Synchrotron Radiation Facility was conceived as a versatile beamline for the study of liquid and solid interfaces, combining grazing-incidence diffraction, X-ray reflectivity and grazing-incidence small-angle scattering in a single instrument. Scattering experiments can be performed both in horizontal and in vertical scattering geometry. Additional options are the use of analyzer crystals for high-resolution studies in both the horizontal and the vertical scattering geometry as well as the use of a horizontal microfocusing mirror for experiments requiring very high flux onto the sample. Here, the way in which the features of the beamline have been exploited in selected recent experiments is described.

© 2005 International Union of Crystallography
Printed in Great Britain – all rights reserved

Keywords: grazing-incidence X-ray scattering; liquid surface scattering; beamline design and instrumentation.

1. Introduction

In recent years there has been an enormous interest in studying organic or biological monolayers and thin films. Studies of self-organization processes in such systems involve length scales from a few nm (monolayers at the air–water interface, self-organized monolayers) to 1000 nm (thin films of polymer blends or block co-polymers), both lateral and normal to the substrate surface. Organic materials are weak scatterers and require high X-ray flux. Therefore studies are frequently carried out at synchrotron radiation sources. However, organic molecules are also prone to radiation damage. This dilemma can often be resolved by exploiting grazing-incidence scattering geometry.

The Troika II beamline (ID10B) at the ESRF was designed to satisfy the needs of a large variety of grazing-incidence scattering experiments with a special emphasis on the study of organic thin films. Both the horizontal scattering geometry as well as the vertical scattering geometry are combined in a single instrument. Whereas the horizontal scattering geometry is exploited for liquid surfaces and heavy sample environments such as *in situ* UHV chambers, the vertical scattering geometry can be used for lightweight sample environments, if large angular access is required. Combining the techniques of grazing-incidence diffraction (GID), X-ray reflectivity (XR) and grazing-incidence small-angle X-ray scattering (GISAXS), length scales from sub-nm to 100 nm, in some cases even up to 1000 nm, have been explored in order to characterize lateral and normal self-organization processes at interfaces and in thin films.

This article is organized as follows. First we describe the beamline optics. Next we provide an overview of the instrumentation in the experimental hutch. We will then present a description of the set-up for XR, GID and GISAXS from liquid surfaces, followed by a description of the vertical scattering geometry. Finally, special options such as high resolution and focusing are presented. The experiment-related sections will be illustrated with experimental results.

2. Beamline optics

The basic beamline optics consists of a horizontal diamond (111) monochromator, a double-bounce mirror for harmonics suppression and various sets of slits (see Fig. 1). The basic idea of the Troika II optics is to provide a very clean high-brilliance X-ray beam to the ID10B experimental hutch.

The beamline is supplied with photons from an ESRF U42 double undulator and a U26 minigap undulator in the common ID10 front-end. All three undulators can be operated in parallel. The first crystal of a diamond (111) double-crystal monochromator acts as a beam splitter deflecting a narrow energy band of radiation towards the second diamond crystal, while the main part of the undulator beam is transmitted downstream to the other Troika experimental stations (I and III). The use of thin diamond crystals of typically 100 µm thickness as beam multiplexers was pioneered at the Troika I beamline (Als-Nielsen *et al.*, 1994). The present beam-splitter crystal has a thickness of 120 µm and the shape of an irregular hexagon with a typical diameter of 10 mm. The crystal yields a transmission between 40% (Troika I at 8 keV on the third

doi:10.1107/S0909049505000361

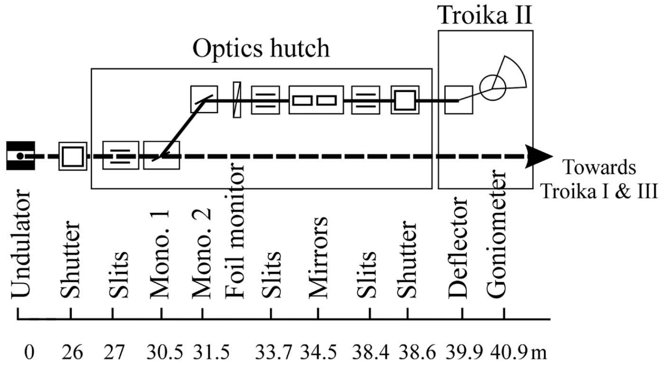

Figure 1
Layout of the Troika II beamline (ID10B) at ESRF. The beam-splitting first diamond crystal deflects beam onto a second diamond crystal at an offset of 850 mm from the main beam. A double-bounce mirror system filters out higher harmonics and allows additional vertical focusing of the beam. Various slit systems clean up the beam from parasitic scattering. The experiments hutch features a beam deflector and a complex multi-purpose diffractometer.

undulator harmonic, Troika II at 13 keV on the fifth undulator harmonic) to 70% (both lines at 9 keV) for the transmitted beam depending on the Bragg angle of the crystal and the undulator harmonics chosen.

The first crystal is housed in an ultra-high-vacuum monochromator developed by the Troika Group (Mattenet *et al.*, 1998) with a residual gas pressure below 10^{-8} mbar. The crystal is in contact with a water-cooled crystal holder using liquid InGa alloy. Since most of the impinging flux from the front-end is transmitted through the crystal, the heat load on the crystal is relatively small, so that the thermal distortion of the crystal in the white beam can be neglected, and simple water cooling of the holder is sufficient (Grübel *et al.*, 1996).

The small Darwin width of diamond (111) amounts to an energy acceptance of only a few eV in the low-divergence undulator beam. Hence both Troika branches (II and I/III) can operate to within 10 eV on the same undulator peak which has typically a full width at half-maximum (FWHM) of 100 eV. This is the most desirable configuration, tripling the available flux at both branches. Similarly, both stations can operate on different undulator harmonics, again providing flux from three undulators at both branches. If photon energy demands at both stations are incompatible, the undulators have to be split up, to supply each branch separately with photons.

The available photon energy range of the Troika II beamline of 8–13.5 keV is given by the travel range of the second diamond (111) crystal. The second diamond crystal is a synthetic diamond supplied by Sumitomo, Japan, and has a thickness of 0.5 mm and an irregular shape with an average diameter of 5 mm. A Bragg–Bragg scattering geometry is used (Grübel *et al.*, 1996). The monochromatic Troika II beam travels parallel to the white beam at a distance of 850 mm in fixed-exit geometry. Because of the large travel range of about 1 m, the crystal goniometer is mounted on a long translation stage inside a He-filled vessel. The goniometer consists of a χ arc to correct the parasitic tilt of the crystal and a θ turntable to align the Bragg angle as well as a small height adjustment of ±2 mm and a horizontal translation of ±5 mm perpendicular to the beam.

For special applications the beamline can be operated on the diamond (333) reflection of the monochromator, yielding an energy range from 24 keV to 40 keV. Line-up is carried out as usual on the third and ninth undulator harmonics. In order to suppress the strong first-harmonic signal from the monochromator, the undulator gaps are successively tuned to the seventh harmonic, which also yields a higher photon flux owing to the stronger magnetic fields at the smaller gap. Despite the overall very critical line-up, the beamline was stable over a week in a pilot experiment at 24 keV.

Ion chambers after the first and the second crystal as well as a beam-finder diode are used to track the beam through the monochromator. Although operating in helium, the response of the ion chamber to the intense monochromatic beam from the first crystal is highly nonlinear, so that they can only be used for rough alignment. The beam finder is a photodiode mounted on the back of the second diamond crystal through an aperture of 1.5 mm. Since the second crystal has a diameter of only 5 mm, the beam finder is very useful for positioning the beam from the first crystal onto the second. Furthermore, the beam finder is used to ensure that the reflected beam from the first crystal lies in the horizontal plane.

The output of the double-crystal monochromator is monitored by a photoelectron monitor consisting of a 3 μm Al foil with a transparency of 99% at 8 keV. The Al foil monitor is mounted insulated on an electric feedthrough in an ultra-high-vacuum cross and the photocurrent is measured with a pA meter. This monitor has a linear response and can also be used to characterize the long-term performance of the monochromator. The top views of both monochromator chambers is provided in Fig. 2.

The next optical element is a double-mirror set-up which filters out higher harmonic contributions, in particular the third harmonic of the monochromator, which coincides with the ninth harmonic of the U42 undulators. Since heat load is negligible in the monochromatic beam, these mirrors can be operated close to the critical angle, maximizing the suppression of higher harmonics, and allowing a short mirror length of only 300 mm. Both mirrors are coated with a platinum strip and a palladium strip. The first mirror, absorbing most of the high energies, has a silicon substrate whereas the second mirror substrate is Pyrex. Each mirror is supported by a three-point mount inside a common ultra-high-vacuum vessel and can be positioned with precision jacks outside the vacuum. The three translations of the jacks are converted to incident angle, sideways tilt and mirror height by the beamline control software. The whole mirror assembly can be shifted perpendicular to the beam, in order to switch between the different coatings. Fig. 3 shows a view into the mirror vessel during installation.

Beam shape and position can be characterized with a beam-position monitor consisting of two crossed 50 μm tungsten wires, one horizontal, one vertical, which can be translated through the beam at 45° from the horizontal plane (Fajardo &

Ferrer, 1995). The photoelectric signal from each wire is picked up by a pA meter.

The Troika II optical system is completed by a set of secondary slits in front of the photon shutter at the downstream end of the common ID10 optics hutch. These slits consist of four independently moveable tantalum blades in a vacuum cross and clean up the beam after the mirror. The bottom blade of the slit assembly features an additional beam stop, in order to stop high-energy spill-over from the first mirror. A schematic overview of the complete optics layout is provided in Fig. 1.

3. Experiments hutch

The equipment in the experiments hutch consists of the beam deflector, the incident flight path and the diffractometer, including various configurations of the detector arm. In the following these components shall be described in detail.

3.1. Beam deflector

The beam deflector is a flexible optical device consisting of a three-axis goniometer and translations in the three perpendicular directions. Its primary function is to deflect the beam downward for scattering studies from liquid surfaces. For small incident angles up to 1°, as used for grazing-incidence diffraction, a 200 mm platinum-coated mirror can be used. For larger deflection angles of up to 7°, a Bragg crystal has to be employed. Because of the highly monochromatic incident beam, a complex goniometer had to be designed which is shown schematically in Fig. 4. The χ arc on top of the θ turntable corrects parasitic tilts in the crystal mount. θ controls the Bragg angle as usual. In order to tilt the exit X-ray beam downward while the incident beam stays at the Bragg angle, the whole assembly can be rotated around the incident beam with the ρ arc. Finally the whole four-stage goniometer is mounted on the φ turntable that aligns the axis of the ρ arc parallel to the X-ray beam. A careful alignment of the assembly is necessary, so that the beam will be reflected properly over the whole angular range.

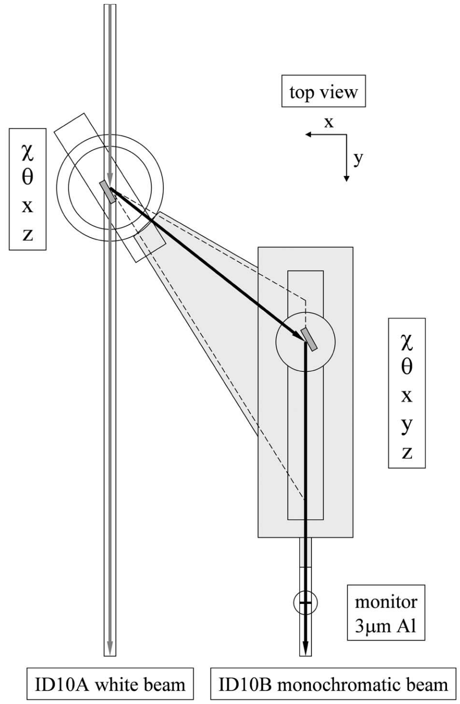

Figure 2
Horizontal fixed-exit monochromator/beamsplitter. The straight-through undulator beam from the ID10 common front-end is depicted on the left (thick solid line), the monochromatic side-beam supplying the Troika II station on the right (thin solid line). Dashed lines indicate the beam positions within the accessible energy range in the second monochromator vessel.

The beam deflection is given by the simple formula

$$\sin(\mu) = \sin(\rho)\sin(2\theta_B).$$

The tilt μ of the X-ray beam with respect to the horizontal plane is a function of ρ, the rotation of the Bragg crystal around the incident beam, and also of the Bragg angle θ_B of the deflector crystal, *i.e.* of the photon energy used. At higher energies (*i.e.* smaller θ_B) the maximum deflection μ_{max} given by the maximum value of ρ of 10° will therefore be smaller. However, at the same time the critical angle for total external reflection from a liquid surface is inversely proportional to the energy which compensates the reduced incident angle. For scattering experiments the proper quantity to consider is the scattering vector $\mathbf{q} = 4\pi/\lambda \sin(\mu)$. Calculation shows that the various energy dependencies for the deflector set-up cancel each other out, so that the maximum $\mathbf{q}$ vector of 0.8 A^{-1} is essentially constant over the energy interval of 8–13.5 keV.

The deflected beam follows the Scherrer cone and thus has also a horizontal deflection σ given by

$$\tan(\sigma) = \sin(\rho)\tan(2\theta_B).$$

For zero deflection, σ equals $2\theta_B$. At maximum deflection using 8 keV photons and a Ge(111) deflector crystal, the deviation from $2\theta_B$ corresponds to 0.35° or a shift of the beam at the scattering center of 6 mm for the ID10B deflector–sample distance of 1 m. Hence the diffractometer has to be able to follow the beam. For this purpose the diffractometer

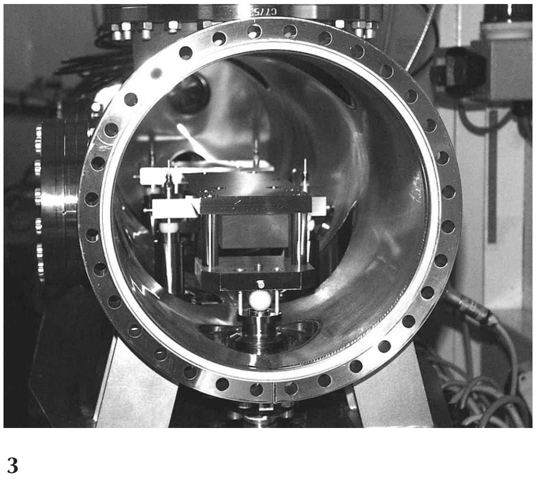

Figure 3
View into the mirror chamber looking upstream. The bounce-down second mirror is seen in the foreground, as it rests on the ceramic spheres of its three-point mount.

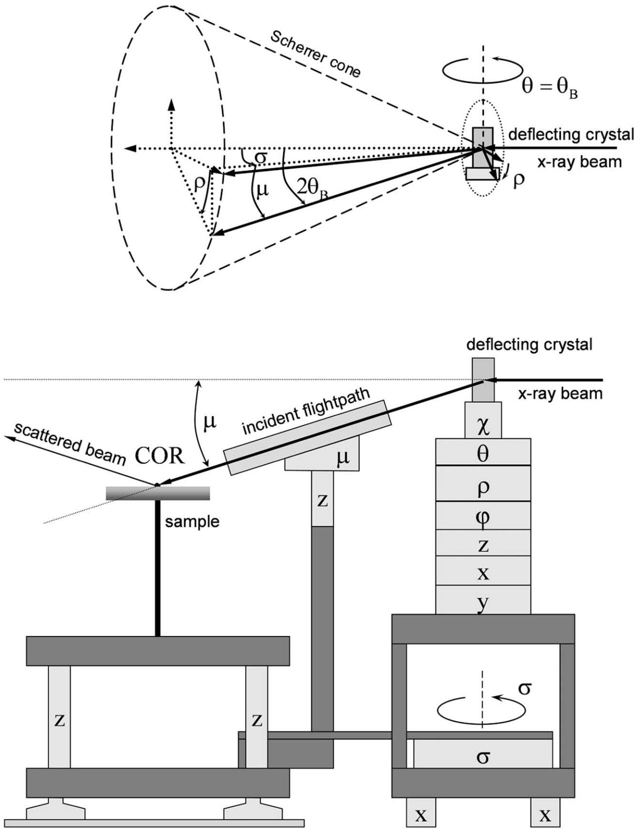

Figure 4
Description of the deflector stage showing angles (top) and components (bottom). The deflecting crystal is adjusted to the Bragg angle $\theta = \theta_B$. In order to deflect the beam out of the horizontal plane, the deflecting crystal is rotated by the angle ρ, while maintaining the Bragg condition with the help of the correction circles χ and φ (see text). The deflected beam moves along the Scherrer cone. The diffractometer center of rotations (COR) follows the deflected beam with the rotation σ, which moves the diffractometer table including the incident flight path on air pads, and a z elevator. The incident flight path also follows the beam with the tilt μ and another z elevator. Additional adjustment translations (x, y, z) on the deflector goniometer allow also a precision alignment of other optical elements such as focusing mirrors, multilayers or X-ray lenses (see text).

table is supported on air pads which glide on a polished marble floor, as it is rotated around the deflector.

Furthermore, the beam height and the angle of the incident flight path as well as the height of the diffractometer table have to follow the tilted incident beam within high precision. If $L_{\rm XF}$ and $L_{\rm XD}$ denote the distances of the flightpath z-translation and the diffractometer center of rotations from the deflector crystal, respectively, the z positions $z_{\rm F}$ of the flightpath and $z_{\rm T}$ of the diffractometer table are given by

$$z_{\rm F} = L_{\rm XF}\tan(\mu), \qquad z_{\rm T} = L_{\rm XD}\tan(\mu),$$

as a function of the tilt angle μ of the X-ray beam from the horizontal plane. The zeros of $z_{\rm F}$ and $z_{\rm T}$ are defined as the positions for the horizontal beam. The tilt of the flightpath $\chi_{\rm F}$ simply follows μ,

$$\chi_{\rm F} = \mu.$$

Within the instrumentation control software *spec* (Swislow, 2004) we have developed a macro that makes all the involved physical motor axes (ρ, $\chi_{\rm F}$, $z_{\rm F}$, σ, $z_{\rm T}$) follow the tilt angle μ. Using this macro, positioning and scanning μ becomes very convenient, as μ appears just like a physical motor axis in the control software.

For our instrument, the deflector–diffractometer distance $L_{\rm XD}$ was chosen to be 1000 mm. The distance $L_{\rm XF}$ between deflector and flightpath is 400 mm. At maximum deflection, the diffractometer table is lowered by 80 mm. The total translation range of the table is from +40 mm to −160 mm with respect to the height of the undeflected beam. The table elevation stage consists of three coupled jacks with a capacity of 2 tons each. A central column with two precision slides prevents a horizontal motion of the table while moving up and down.

3.2. Incident flight path

The incident flight path comprises an evacuated tube with the incident slit, the incident beam monitor and an attenuator wheel close to the sample. The incident slits are motorized Huber slits using a home-built design that allows easy access and exchange of components. For further collimation, a second pair of motorized slits can be set up at the entrance of the flight path. The incident beam intensity is monitored by a Kapton detector in which beam scattered at 90° by a 80 µm Kapton foil is detected with a scintillation detector. Variable apertures in front of the detector ranging from 0.5 mm to 2 mm diameter allow adjustment of the scattered photon flux to the dynamic range of the detector.

The final optical element in the flight path is an aluminium attenuator wheel consisting of 20 slots with absorber thicknesses ranging from 0 to 1.9 mm in steps of 0.1 mm. The attenuator has proven to be a very valuable tool in keeping the radiation dose onto sensitive organic samples to a minimum during line-up. Once samples are lined up in grazing-incidence geometry, the attenuation can be safely removed. Similarly, the detectors can be protected when lining up the sample on bulk Bragg reflections. Finally the motorized attenuator is indispensable for reflectivity measurements.

3.3. Diffractometer

The design of the ID10B diffractometer was based on two important considerations: the instrument should be able to make use both of the horizontal as well as of the vertical scattering geometry and there should be ample space for bulky sample environments such as Langmuir troughs or *in situ* vacuum chambers. Furthermore, both diffractometer and deflector unit had to fit into a limited space as defined by the clearance between white-beam transfer pipe and the monochromatic ID10B photon beam of about 750 mm as well as the relatively short length of the experimental hutch of only 2.5 m in the beam direction.

Our choice of diffractometer configuration was influenced by the Troika I diffractometer, originally conceived as a liquid scattering diffractometer, and the multipurpose diffractometer at ESRF beamline BM32. We chose the spaciousness of the former and the compact configuration of circles of the latter. The resulting custom ID10B diffractometer by Huber Diffraktionstechnik (Huber, http://www.xhuber.com) is depicted in Fig. 5 in two side views, one perpendicular to the X-ray beam and the other along the beam direction showing rotation axes and translations. Fig. 6 presents a three-dimensional view. The most prominent feature is the two-component detector arm which has a γ circle moving the detector in the vertical scattering plane which is mounted on the horizontal δ turntable. The sturdy design permits a maximum of 17 kg for detector and flight path to be put onto the counterweighted γ arm. Additionally, the detector arm was equipped with connectors for ten auxiliary motor channels which can be used for controlling motorized slits or analyzer stages.

The horizontal sample stage consists of the θ turntable, a $z_{\rm H}$ translation controlling the sample height in the beam and crossed arcs φ and χ to align the surface normal. Additional horizontal translations $x_{\rm H}$ and $y_{\rm H}$ can be provided, reducing the distance between the top of the sample goniometer to the sample position from 170 mm to 110 mm. All components are heavy duty and can support up to 150 kg of sample environment. The space on this stage is sufficient to support a 200 mm × 800 mm Langmuir trough (Daillant, 1999) including an active vibration-damping system or an ultra-high-vacuum chamber for *in situ* growth studies (Ritley *et al.*, 2001).

In combination with a down-deflected beam (angle μ), the horizontal scattering geometry corresponds to the z-axis geometry (Lohmeier & Vlieg, 1993). This mode is supported in the *sixc* version of the *spec* instrument control software (Swislow, 2004). Angular access in the horizontal scattering geometry is somewhat restricted by the vertical sample stage colliding with the detector arm or the incident flight path, so that careful setting of absolute and relative motor limits is mandatory. Unless there are further restrictions imposed by the sample environment, the available θ range is between -40° and $+40^\circ$.

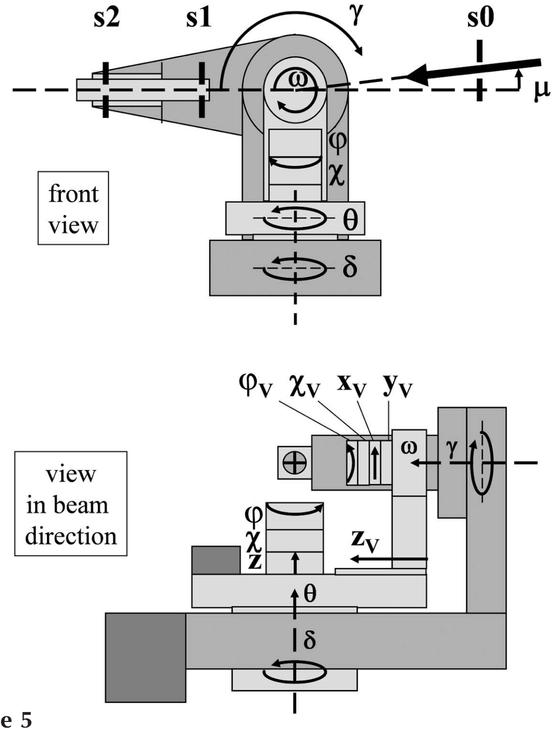

Figure 5
Schematic side view (top) and view along the beam (bottom) of the Troika II diffractometer. Rotation axes and translations are indicated. For details see text.

A second sample stage used for the vertical scattering geometry has an additional ω turntable rotating the sample around its surface normal. The incident angle is controlled by the θ turntable in this case. This so-called 2 + 2 geometry has been independently developed by Ken Evans-Lutterodt (Evans-Lutterodt & Tang, 1995) and Gilles Renaud (Renaud *et al.*, 1995) and allows a very compact surface diffractometer to be built with perfect control of the incident angle and maximum angular access for the sample azimuth and detector. Further features of the vertical sample stage are a motorized goniometer comprising crossed arcs $\varphi_{\rm V}$ and $\chi_{\rm V}$, and sideways translations $x_{\rm V}$ and $y_{\rm V}$. The $z_{\rm V}$ translation in the direction of the sample normal positions the sample precisely into the beam. With the crossed arcs, a precise alignment of the surface normal with respect to the ω axis can be achieved.

The vertical sample stage features a spacing of 110 mm between the mounting plate and the sample position. It can support small sample cells with a weight of up to 2 kg. The long translation $z_{\rm V}$ of +10 mm and -150 mm can be used to remove the vertical sample stage away from the center of the instrument, in order to make space for bulky equipment to be mounted on the horizontal sample stage.

The 2 + 2 scattering geometry is supported by *spec* code *w21v* [for general information see Swislow (2004)]. For ID10B a custom version of this code was provided which uses the *sixc* motor names for detector arm (γ, δ) and sample rotation (θ)

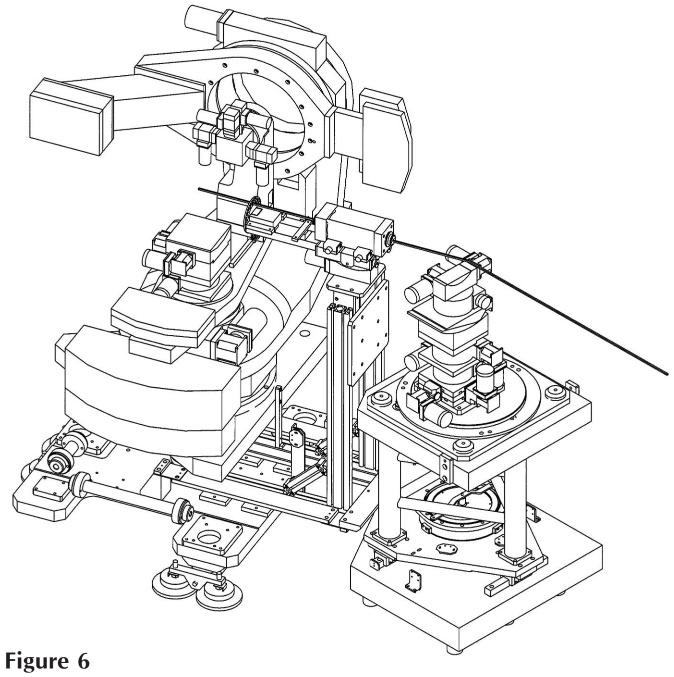

Figure 6
Three-dimensional view of the diffractometer, incident flight path and beam deflector.

and introduces one additional sample rotation ω. In this way, confusion on motor names, when changing scattering geometry, is avoided. The 2 + 2 geometry is as powerful as the vertical z-axis geometry, with the added virtue of a more compact arrangement of motor axes (Evans-Lutterodt & Tang, 1995; Renaud *et al.*, 1995; Smilgies, 2002). A three-dimensional view of diffractometer and deflector is given in Fig. 6.

For the line-up of the diffractometer with respect to the incident X-ray beam, *i.e.* in order to put the beam into the center of rotations of the instrument, a line-up pinhole of diameter 1 mm is mounted on the vertical sample stage. By rotating ω and θ by 180° the center of rotations can be accurately determined with the cross-hair of a line-up telescope. In the next step, beam and diffractometer are positioned such that the beam passes through the pinhole. For this purpose the diffractometer table can be translated vertically and horizontally perpendicular to the beam. Alternatively, the horizontal beam position can also be controlled with the sideways translation of the second monochromator crystal. Finally, the zeros of the detector arm angles γ and δ are obtained by lining up the detector arm on the beam passing through the pinhole. As the final step, all remaining slits are centered around the X-ray beam and set to the desired resolution.

3.4. Detector arm configurations

The standard detector arm set-up comprises a Newport X48 optical bench that can host various components. The default detector arm configuration is a scintillation detector in combination with two pairs of motorized slits. The detector slit typically has a distance of 700 mm from the center of the instrument. The entrance slit can be as close as the sample environment permits; however, it is typically put at 200 mm from the center of rotations for convenience. Between the slits there is an evacuated flight path with Kapton windows. The detector can also be operated as a Kapton detector by moving it into a second housing at 90° with respect to the beam and inserting a Kapton scattering foil in the beam path. The latter set-up is very useful for line-up of the instrument on the direct beam. As an additional option, a 20 mm × 20 mm Soller slit with 0.2° resolution (Huber) can be mounted.

The second detector arm configuration is for use with linear gas detectors. There are two types of linear gas detectors available: a 50 mm detector by MBraun (MBraun, http://www.mbraun.com) with a resolution of 80 µm, and a 150 mm Gabriel detector (EMBL, European Molecular Biology Laboratory, Grenoble, France) with a resolution of 200 µm. Both detectors can be mounted on the X48 optical bench. The MBraun detector can be combined with a rectangular flight path in horizontal or in vertical orientation and a motorized Huber slit as entrance slit. Fixed apertures of various widths over the full height are placed in front of the detector aperture to define the perpendicular resolution. The Gabriel detector can be mounted both vertically and horizontally. In the vertical configuration it can be combined with a 150 mm × 15 mm Soller slit by JJ X-ray with a resolution of 1.4 mrad (JJ X-ray, http://www.jjxray.dk) or a home-built long collimator with fixed slits on either end. The entrance slit of the long collimator can be aligned with the help of a motorized translation.

The optical bench can be replaced by a compact home-built analyzer stage (Smilgies, 2003). This light-weight set-up comprises two modified Huber 408 turntables. The central column of the lower turntable supports a small motorized Kohzu arc with an angular range of ±10°, on which various analyzer crystals can be mounted. The upper turntable supports the detector. Mounts for all beamline detector types are provided. The analyzer stage can be configured for both a vertical or a horizontal scattering geometry for the scintillation detector and the MBraun detector. The larger and heavier Gabriel detector can be only used in horizontal scattering geometry. For combination with the Gabriel detector, a 150 mm × 40 mm Si(111) analyzer crystal was provided by the crystal laboratory of the ESRF Optics Group. Other available crystals are 60 mm × 40 mm Si(111) and Ge(111) crystals as well as a matched pair of asymmetric-cut Si(111) crystals with b parameters of 10 and 0.1 at 9 keV. Fig. 7 shows a photograph of the analyzer stage in vertical scattering geometry.

4. Liquid scattering set-up

Liquid scattering, in particular liquid reflectometry on a synchrotron beamline, constitutes one of the most challenging instrumentation problems in X-ray scattering involving the precise motion of half a dozen motors, as detailed in §3.1 (in particular see Fig. 4). Nonetheless, it is extremely useful to be able to combine GID from liquid surfaces with XR on the same instrument.

Various kinds of Langmuir troughs can be used at Troika II. The beamline is equipped with a copy of the Langmuir trough developed by the Saclay group (Daillant, 1999). This trough has a length of 400 mm and a width of 170 mm which allows a

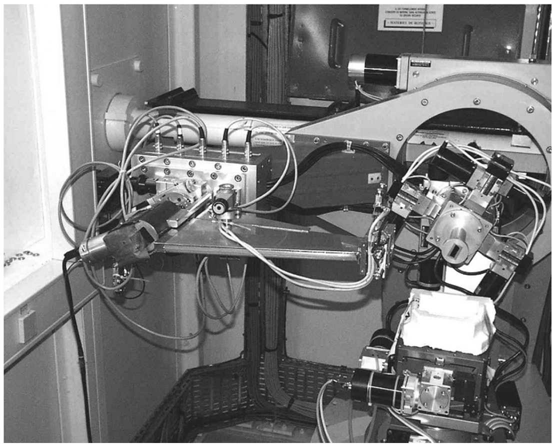

Figure 7
Detector arm configured with the analyzer stage in the vertical scattering geometry and a Cyberstar scintillation detector. At the entrance of the triangular flight path, motorized slits can by adjusted for optimum background suppression. This flight path can also be used in combination with a linear gas detector. The detector arm features ten flexible motor channels for slit and analyzer motions.

150 mm footprint of the beam. Compression of monolayers can be achieved with a solid barrier yielding a maximum compression rate of 6. The surface pressure is measured with a Wilhelmy balance (Riegler & Kirstein, http://www.rieglerkirstein.de). Analog signals for the pressure can be logged *via* analog-to-digital converters by the instrument control program *spec* (Swislow, 2004). Set points for the pressure feedback can be provided with a digital-to-analog converter, whereas the trough temperature is stabilized to within 0.1 K with a close-circuit chiller, which is presently controlled manually. The trough is supported by an active vibration-damping system (Halcyonics, http://www.halcyonics.de), in order to compensate for vibrations when diffractometer motors are moving.

For precious samples like proteins or peptides a small Teflon trough of diameter 100 mm is used. For the diffuse measurements of the capillary wave dynamic of liquid surfaces, a large round trough of diameter 300 mm was specifically designed by the Saclay group (Fradin *et al.*, 2000). These experiments benefited particularly from the low background in the Troika II hutch. High-resolution measurements of phase transitions in fatty alcohols were performed in a doubly insulated trough by the Grenoble group (Zakri *et al.*, 1997; Alonso *et al.*, 2001), in combination with the Troika II analyzer stage (Smilgies, 2003).

As an example of the combined use of reflectivity and GID we present results from a study by Konovalov *et al.* of the interaction of antimicrobial peptides with phospholipid monolayers spread at the air–water interface (Konovalov *et al.*, 2002). Phospholipids are main components of the cell membrane. When spread on the water surface, they form oriented two-dimensional ordered structures which are used to mimic half of a cell membrane. The outer surface of prokaryotic cell membranes is composed of negatively charged phosphatidylglycerol lipids such as DSPG whereas the outside of eukaryotic cell membranes is composed of zwitterionic phosphatidylcholine lipids such as DSPC. Antimicrobial peptides are able to discriminate between these differences in cell membrane architecture and selectively kill pathogenic micro-organisms.

XR and GID provide structural information normal to the film and in the surface plane, respectively, on an atomic length scale. Fig. 8 shows the ⟨111⟩ in-plane Bragg peaks of DSPC (zwitterionic) and DSPG (negatively charged) phospholipids monolayers at different surface pressures with and without the presence of the antimicrobial peptide peptidyl-glycyl-leucine-carboxyamide (PGLa). PGLa was isolated from the skin of the South African clawed frog, *Xenopus laevis*, and consists of 21 amino acids (Andreu *et al.*, 1985). The scattering results clearly show that PGLa does not affect the structural organization of the DSPC layer, because the Bragg peak position (corresponding to the two-dimensional lattice parameters) and its width (characterizing the average domain size) remain intact. In contrast, the structure of a DSPG layer is destroyed at contact with PGLa.

In case of a lack of two-dimensional long-range order, such as for the same system at surface pressures below 15 mN m^{-1}, the only way to study the structure of a DSPG/PGLa mixture

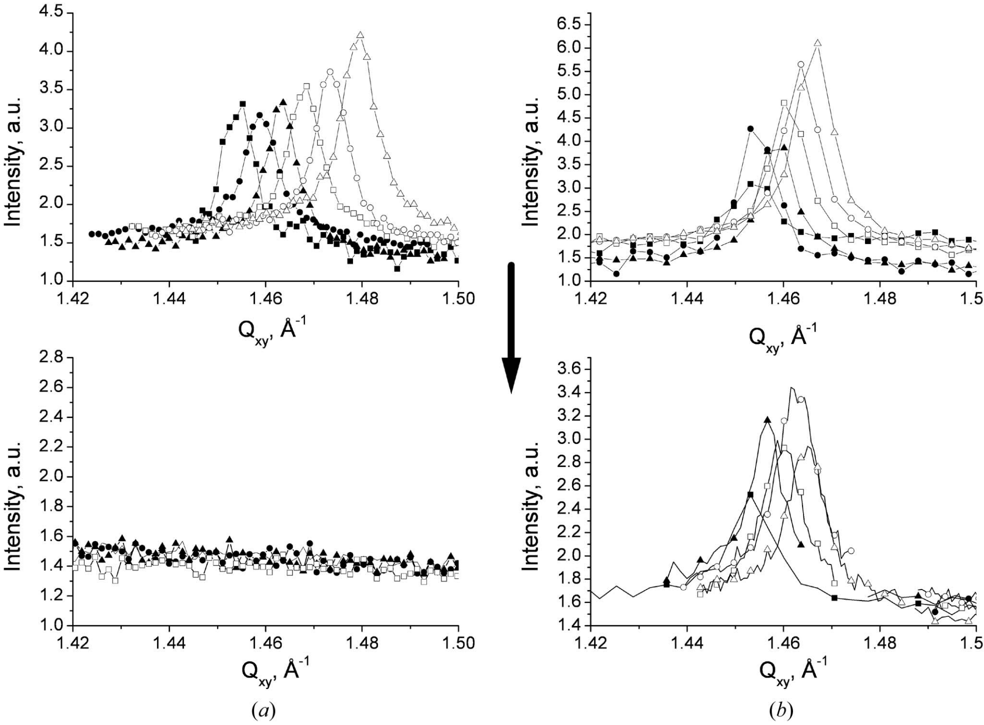

(*a*) (*b*)

Figure 8

Grazing-incidence diffraction spectra of monolayers of DSPG (*a*) and DSPC (*b*) without (top) and with (bottom) the presence of PGLa peptide at different surface pressures [15 mN m^{-1} (black squares), 20 mN m^{-1} (black circles), 25 mN m^{-1} (black triangles), 30 mN m^{-1} (white squares), 35 mN m^{-1} (white circles), 40 mN m^{-1} (white triangles)]; aqueous subphase: 10 m*M* Na-phosphate, pH 7.4. Reprinted from Konovalov *et al.* (2002) with permission from Springer Verlag.

is reflectivity (Fig. 9). It was found that DSPG and PGLa mix on the molecular level forming a homogeneous layer without any long-range order, whereas the reflectivity from a mixture of DSPC and PGLa (Fig. 9) indicated a two-phase system in the film which we interpret as domains of DSPC and PGLa coexisting at the air–water interface.

Apart from XR and GID, the experimental set-up also supports non-specular scattering from liquid surfaces. Rocking scans and detector scans can be performed by choosing appropriate incident angles (with the deflector stage) and exit angles (with the γ-arm of the diffractometer, if used with a point detector, or using a linear gas detector).

5. Vertical scattering geometry

The vertical scattering geometry is the classic geometry for crystallography of solid surfaces (Feidenhans'l, 1989; Robinson & Tweet, 1992). In-plane scattering, *i.e.* when the scattering vector is parallel to the surface, is not affected by the polarization factor, which is of advantage when large in-plane data sets for surface crystallography are to be recorded. In contrast, rod scans, *i.e.* scans along the normal component of the scattering vector, are affected by the linear polarization of synchrotron radiation (Smilgies, 2002). Rod scans provide information on the ordering perpendicular to the surface, thus allowing a full three-dimensional characterization of surface structures, thin films and nano-objects such as quantum dots.

As an example for the use of this diffractometer mode we show results obtained by Smilgies *et al.* (2000) to characterize single-crystalline films of the molecule 1,4-bis(5-phenyloxazol-2-yl)benzene (POPOP) grown on KCl (001) substrates. POPOP is a molecule with intense fluorescence and electrofluorescence and interesting for electro-optical devices. The molecules grow in the shape of long needles in preferential directions on the substrate. In this study it was found that POPOP crystallites feature the monoclinic bulk structure and grow with their (201) face parallel to the substrate surface [Fig. IV.1 of Smilgies *et al.* (2000)]. The long molecular needles grow in the POPOP [010] direction and are oriented along the [110] direction of the substrate (Smilgies *et al.*, 2000). A distinctive feature of the film texture are 180° domains owing to the monoclinic molecular lattice which constitute a basic growth defect that would even prevail on substrates of lower symmetry than the cubic KCl (001) substrates used here (Fig. 10).

The technique has been extended to systematic texture studies of other molecular films (Kintzel *et al.*, 2001; Smilgies *et al.*, 2002) interesting for applications in molecular electronics. High-quality single-crystalline organic materials are expected to feature unprecedented electronic transport properties compared with previously known thin-film materials. A major challenge in the molecular electronics field will be to grow thin films of similar quality for device applications. Grazing-incidence diffraction provides detailed information on the film morphology, in order to establish optimal growth parameters.

A second example of the successful application of the vertical 2 + 2 scattering geometry was structural studies of self-assembled InAs quantum dots, grown by molecular beam epitaxy on GaAs (001). In such quantum dots the electrons are confined in all three directions of space, and the opto-electronic properties depend on the size and chemical composition

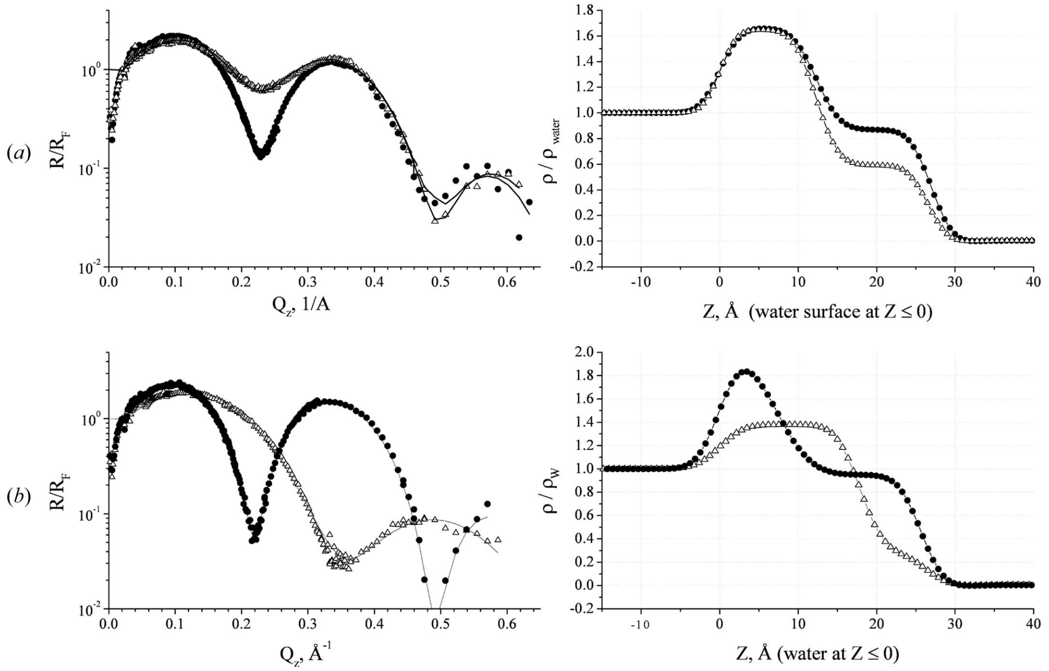

Figure 9
Measured (symbols) and fitted (lines) Fresnel normalized X-ray reflectivities of lipid monolayers and their mixtures with the PGLa peptide at a surface pressure of 15 mN m^{-1} are shown on the left-hand side. The corresponding scattering length density profiles are given on the right-hand side of the figure. (*a*) DSPC (white circles) and mixture of DSPC/PGLa (white triangles); (*b*) DSPG (white circles) and mixture of DSPG/PGLa (white triangles). Both mixtures are at a concentration 1:1 wt/wt. Reprinted from Konovalov *et al.* (2002) with permission from Springer Verlag.

of the dots as well as on the internal strain owing to the lattice mismatch with the substrate. Hence, the determination of interdiffusion and strain profiles within quantum dots is of paramount importance for the understanding of the growth process and for the prediction of device properties. Measurements in grazing-incidence and grazing-exit diffraction performed at the ID10B beamline by Metzger and collaborators (Kegel *et al.*, 2000, 2001) allowed three-dimensional intensity maps of selected regions in reciprocal space to be obtained, from which the shape, strain and composition of the dots could be reconstructed. In addition to a monotonic variation of the lattice parameter from the bottom to the top, the material composition was found to vary continuously from pure GaAs at the base of the dots to pure InAs at the top. Only the combination of both measurements guaranteed an accurate determination of the lattice strain inside the dots.

6. Special options

The beamline can be configured into a high-resolution set-up or a focusing set-up for specific applications. In the high-resolution set-up, crystal optics is used to increase the resolution over that obtained with slits. In the focusing mode the undulator beam is focused horizontally, in order to increase the flux onto a sample under grazing incidence.

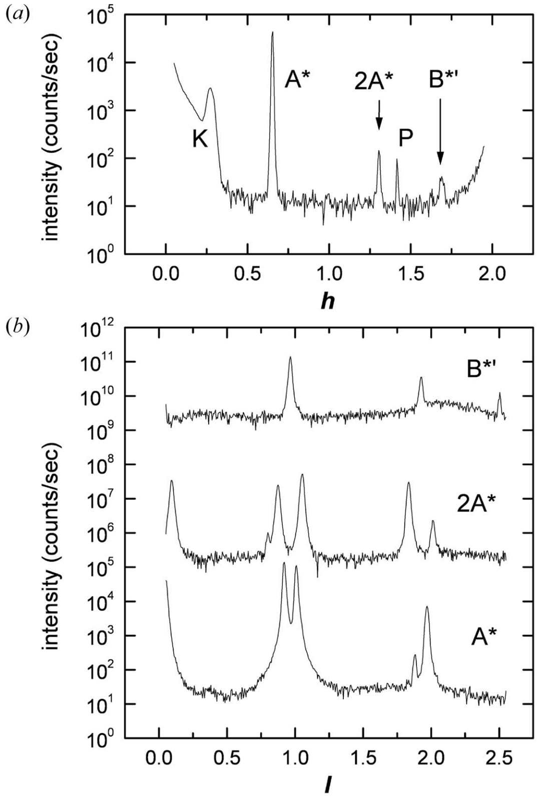

Figure 10
Grazing-incidence diffraction in the vertical scattering geometry of an in-plane scan (*a*) and rod scans (*b*) from a POPOP film grown on a KCl (001) substrate. The characteristic monoclinic splitting of the POPOP Bragg reflections in the scattering rods marked with A* and 2A* is due to the formation of 180° domains in the molecular film, whereas the scattering rod in the special direction B*′ is not split. Needle-like POPOP domains line up with the substrate [110] high-symmetry directions. Reprinted from Smilgies *et al.* (2000) with permission from Elsevier.

6.1. High-resolution mode

For experiments requiring a higher resolution than can be obtained with slits, crystal optics can be used. An analyzer crystal is essentially an optical element that accepts a small angular range as given by the Darwin width and the mosaic spread of the analyzer crystal. The trade-off between the use of slits *versus* analyzer crystals is that at some point closing the slits will reduce the intensity so much that the small angular acceptance of a Si(111) crystal in the full beam yields a higher signal on the detector than can be achieved with corresponding slit settings. At 8 keV the measured rocking width of the Si(111) crystals used at ID10B was of the order of 0.005°, which is slightly larger than the calculated Darwin width of 0.003°. The additional spread is ascribed to the divergence of the incident beam and some residual mosaicity of the almost perfect analyzer crystal.

The flexible analyzer set-up can be operated both in the horizontal and the vertical scattering geometry. In the horizontal geometry the analyzer Bragg angle lies in the horizontal plane. This way, surface structures at the air–water interface can be analyzed at very high resolution. An example are monolayers of chiral fatty alcohols analyzed by Renault and collaborators (Zakri *et al.*, 1997; Alonso *et al.*, 2001). From a careful line shape analysis the microscopic elasticity constants such as compressibility and shear modulus can be derived, which are not available from macroscopic direct measurements since the grain structure dominates the macroscopic elastic properties. For this experiment, an analyzer crystal of height 150 mm was combined with a linear gas detector of similar height so that a large range of exit angles could be detected at each point of an in-plane scan (Smilgies, 2003).

A second experimental application of the horizontal analyzer stage was a GISAXS study of roughness correlations in ultra-thin films of polymers and polymer blends. The decay of the correlated roughness oscillations with the parallel scattering vector $\mathbf{q}_{\|}$ provides direct information on the degree in which the polymer film can follow the surface topography of the solid substrate (Gutmann *et al.*, 2000). For this purpose the silicon substrates were deliberately roughened by etching. This treatment reduced also the specular reflectivity of the substrate, so that the reflected beam at 1.5° incident angle could be accepted by the detector system without attenuation, while the diffuse correlated roughness oscillations were hardly affected. In this experiment, again the combination of a 150 mm-high Si(111) analyzer crystal with a linear gas detector of matching size (Smilgies, 2003) was exploited. Our set-up was ideally suited to the very anisotropic scattering geometry scanning an in-plane scattering angle range of only 0.1°, while recording an exit angle range of 0 to 5° containing the full oscillation pattern. The decay of the roughness oscillations revealed that typical cut-off lengths are of the order of 100 nm, *i.e.* the polymer films do not follow any surface roughness features on length scales below this cut-off length (Gutmann *et al.*, 2000).

A further increase in resolution can be achieved by conditioning the incident beam with an asymmetric-cut crystal. A silicon single crystal with an asymmetric cut of 10.44° off the (111) plane was cut and polished in the Crystal Laboratory of the ESRF Optics Group. At an energy of 9 keV the asymmetry parameter b of this crystal (Als-Nielsen & McMorrow, 2001) equals 0.10, *i.e.* the incident beam is broadened by a factor of $1/b = 10$, while its divergence is reduced by a factor of $b^{1/2} \simeq 1/3$. Note that the acceptance of this crystal is enhanced by a factor of $b^{-1/2} \simeq 3$ as compared with a symmetric-cut Si(111), and thus the full beam divergence from the horizontal diamond (111) monochromator is accepted. The widening of the beam has the additional benefit that the energy density of the beam becomes spread out, thus reducing the radiation damage in sensitive samples.

The analyzer can be equipped with a matching asymmetric-cut Si(111) crystal with $b = 10$ at 9 keV which has a narrow measured acceptance of 0.002°. Additionally, the second crystal condenses the broad beam from the first crystal for detection with a scintillation detector or a linear gas detector. The whole set-up can achieve a resolution of length scales up to 10000 Å. A first demonstration has been given by Papadakis and co-workers in their GISAXS study of lateral structures in thin films of diblock copolymers. Film Bragg peaks corresponding to a lamellar period of 850 Å were easily resolved (Smilgies, 2003; Busch *et al.*, 2005).

In the vertical scattering geometry, the analyzer set-up, in combination with both the scintillation detector and the small 50 mm linear gas detector, has been utilized for high-resolution experiments on solid surfaces. Particularly pretty results were obtained by Jenichen *et al.* in their study of a quantum wire gratings on InP(001) obtained by wet etching after electron beam lithography. The diffraction map depicted in Fig. 11 reveals both the grating period of 120 nm as well as diffuse streaks perpendicular to the tilted side planes of this trapezoidal grating. Owing to the high aspect ratio, such gratings are very difficult to image directly using scanning probe techniques. The detailed analysis of the diffraction intensities reveals the residual strain fields in and around the 35 nm-broad and 8 nm-thick InGaAsP quantum wires (near 1% compressive strain) after the etching process (Kaganer *et al.*, 2002).

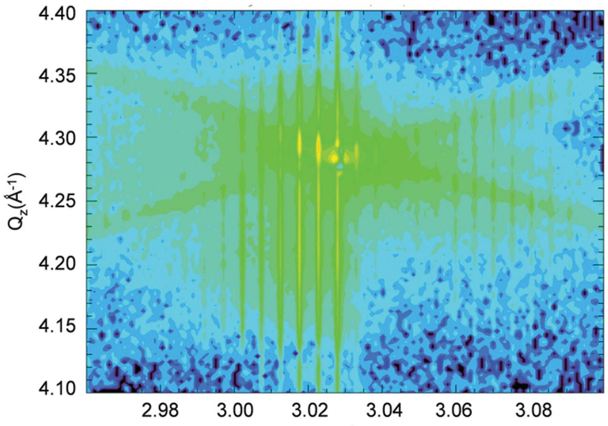

Figure 11
High-resolution diffraction from a lithographically prepared free-standing grating of period 120 nm. The fine vertical streaks indicate the grating period, whereas the weak oblique streaks are due to scattering from the sides of the trapezoidal ridges. From the intensity distribution in the streaks, residual strain fields in the grating after etching can be determined. Reprinted from Kaganer *et al.* (2002) with permission from the American Physical Society.

6.2. Focusing mode

The beamline can be operated in a focusing mode yielding a very high incident flux onto the sample, when a graded multilayer bender provided by the ESRF Optics Group is used. The bender focuses the full horizontal beam width of 1 mm FWHM down to 25 µm, according to a 40:1 demagnification ratio. The meridionally focusing Mo:B_4C multilayer has a graded lattice constant, so that the beam is intercepted under the local Bragg angle along the full length of the 150 mm substrate.

For a typical sample size of 10 mm diameter and incident angles of the order of 0.2°, the effective horizontal cross section of the sample is matched to the focused beam width, *i.e.* the full undulator beam illuminates the sample under grazing incidence. At a distance of 1 m from the sample, the resulting divergence of the focused beam is of the order of 1 mrad. The increased horizontal divergence of the focused beam is acceptable, as long as the incident angle is still defined reasonably, *i.e.* if it is larger than about 2 mrad, which corresponds to the critical angle of water at 10 keV. For the vertical scattering geometry, the direction of reduced resolution is matched up with diffuse scattering perpendicular to the surface, *i.e.* at little sacrifice to the resolution.

A successful demonstration of this high-flux geometry has been given in a recent experiment by de Jeu and co-workers at ID10B. A free-standing smectic liquid-crystalline film of only seven layers was mounted in a vertical frame and illuminated under an incident angle of 0.6° (about three times the critical angle). The beam was focused at the sample. Grazing-incidence diffraction was performed in reflection mode using a linear detector in the scattering plane (see Fig. 12). This way the line shape associated with the positional ordering inside the liquid-crystal layers could be caught in a single shot and the fluid-to-hexatic-to-crystalline phase transitions in the top layer could be followed (Chao *et al.*, 1996; Fera *et al.*, 1999; de Jeu *et al.*, 2003).

As studies with microfocused beams are becoming increasingly important, other focusing elements like Fresnel lenses or compound refractive lenses can be mounted and aligned on the deflector stage in a straightforward way.

7. Conclusion

The Troika II beamline at ESRF (ID10B) has shown to be a very versatile beamline for scattering from soft-matter and hard-matter surfaces and thin films. The optics features

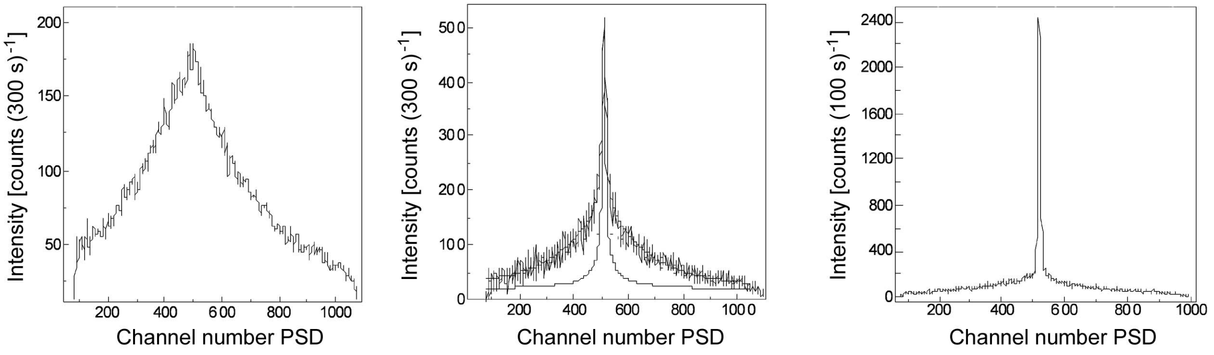

(*a*) (*b*) (*c*)

Figure 12

Scattering from a free-standing film of the liquid crystal 4O.8 showing raw data for the in-plane diffraction peak of a seven-layer smectic membrane. As the temperature is lowered, the top layers undergo a liquid-to-hexatic-to-crystalline transition [as shown in panels (*a*), (*b*) and (*c*), respectively], whereas the inner layers remain in the liquid state. The combination of horizontal focusing with the ID10B multilayer bender with a linear detector was crucial for this experiment. Reprinted from de Jeu *et al.* (2003) with permission from the American Physical Society.

pioneering X-ray beam multiplexing of undulator beams in the 10 keV photon energy range. A very clean X-ray beam for high-resolution and low-background experiments is available. The experimental station supports various scattering geometries for both *ex situ* and *in situ* sample environments and can be adapted to differing resolution and incident flux requirements.

We are indebted to Gerhard Grübel whose constant support and advice was invaluable in building the Troika II beamline. Without the continuing efforts of Patrick Feder and Henri Gleyzolle this station could not have been realised. Special thanks to the ESRF Optics Group, providing us with miraculous devices, in particular the diamond beam splitter, the multilayer bender and the large analyzer crystal. The beamline was essentially home-built by the ingenuous design work of Muriel Mattenet, Keith Martel, Yves Gibert, Jürgen Kapfhamer and Thomas Schneider at ESRF. We thank Norman Huber for the close coordination of the custom diffractometer design at Huber Diffraktionstechnik GmbH with our in-house efforts and providing a first-rate instrument. Finally we would like to thank the in-house support groups at ESRF for their contributions in constructing the beamline. We are very grateful for many valuable suggestions provided by the Troika II user community during the first years of operation. Special thanks to Bernd Jenichen and Wim de Jeu for contributing figures highlighting some of the special features of the beamline. DMS acknowledges financial support by the CHESS Center at Cornell University.

References

Alonso, C., Artzner, F., Suchod, B., Berthault, M., Konovalov, O., Pecaut, J., Smilgies, D. & Renault, A. (2001). *J. Phys. Chem. B*, **105**, 12778–12785.

Als-Nielsen, J., Freund, A. K., Grübel, G., Linderholm, J., Nielsen, M., Sanchez del Rio, M. & Sellschop, J. P. F. (1994). *Nucl. Instrum. Methods Phys. Res. B*, **94**, 306–318.

Als-Nielsen, J. & McMorrow, D. F. (2001). *Elements of Modern X-ray Physics*, p. 318. Germany: Wiley-VCH.

Andreu, D., Aschauer, H., Kreil, G. & Merrifield, R. B. (1985). *Eur. J. Biochem.* **149**, 531–535.

Busch, P., Smilgies, D.-M., Posselt, D. & Papadakis, C. M. (2005). In preparation.

Chao, C.-Y., Chou, C.-F., Ho, J. T., Hui, S. W., Jin, A. & Huang, C. C. (1996). *Phys. Rev. Lett.* **77**, 2750–2753.

Daillant, J. (1999). *Synchrotron Rad. News*, **12**, 17–23.

Evans-Lutterodt, K. & Tang, M.-T. (1995). *J. Appl. Cryst.* **28**, 318–326.

Fajardo, P. & Ferrer, S. (1995). *Rev. Sci. Instrum.* **66**, 1882–1884.

Feidenhans'l, R. (1989). *Surf. Sci. Rep.* **10**, 105–188.

Fera, A., Ostrovskii, B. I., Sentenac, D., Samoilenko, I. & de Jeu, W. H. (1999). *Phys. Rev. E*, **60**, R5033–R5036.

Fradin, C., Braslau, A., Luzet, D., Smilgies, D., Alba, M., Boudet, N., Mecke, K. & Daillant, J. (2000). *Nature (London)*, **403**, 871–874.

Grübel, G., Abernathy, D., Vignaud, G., Sanchez del Rio, M. & Freund, A. (1996). *Rev. Sci. Instrum.* **67**, 1–4.

Gutmann, J. S., Müller-Buschbaum, P., Schubert, D. W., Stribeck, N., Smilgies, D. & Stamm, M. (2000). *Physica B*, **283**, 40–44.

Jeu, W. H. de, Fera, A., Konovalov, O. & Ostrovskii, B. I. (2003). *Phys. Rev. E*, **67**, 020701(R)-1–020701(R)-4.

Kaganer, V. M., Jenichen, B., Paris, G., Ploog, K. H., Konovalov, O. & Mikulik, P. (2002). *Phys. Rev. B*, **66**, 035310-1–035310-7.

Kegel, I., Metzger, T. H., Lorke, A., Peisl, J., Stangl, J., Bauer, G., Garcia, J. M. & Petroff, P. M. (2000). *Phys. Rev. Lett.* **85**, 1694–1697.

Kegel, I., Metzger, T. H., Lorke, A., Peisl, J., Stangl, J., Bauer, G., Nordlund, K., Schoenfeld, W. V. & Petroff, P. M. (2001). *Phys. Rev. B*, **63**, 035318-1–035318-13.

Kintzel, E. J. Jr, Smilgies, D.-M., Skofronick, J. G., Safron, S. A., Van Winkle, D. H., Trelenberg, T. W., Akhadov, E. A. & Flaherty, F. A. (2001). *J. Vac. Sci. Technol. A*, **19**, 1270–1276.

Konovalov, O., Myagkov, I., Struth, B. & Lohner, K. (2002). *Eur. Biophys. J.* **31**, 428–437.

Lohmeier, M. & Vlieg, E. (1993). *J. Appl. Cryst.* **26**, 706–716.

Mattenet, M., Schneider, T. & Grübel, G. (1998). *J. Synchrotron Rad.* **5**, 651–653.

Renaud, G., Villette, B. & Guénard, P. (1995). *Nucl. Instrum. Methods Phys. Res. B*, **95**, 422–430.

Ritley, K. A., Krause, B., Schreiber, F. & Dosch, H. (2001). *Rev. Sci. Instrum.* **72**, 1453–1457.

Robinson, I. K. & Tweet, D. (1992). *Rep. Prog. Phys.* **55**, 599–651.

Smilgies, D.-M. (2002). *Rev. Sci. Instrum.* **73**, 1706–1710.

Smilgies, D.-M. (2003). *Rev. Sci. Instrum.* **74**, 4041–4047.

Smilgies, D.-M., Boudet, N., Struth, B., Yamada, Y. & Yanagi, H. (2000). *J. Cryst. Growth*, **220**, 88–95.

Smilgies, D.-M., Boudet, N. & Yanagi, H. (2002). *Appl. Surf. Sci.* **189**, 24–30.

Swislow, G. (2004). *spec* on-line manual (Certified Scientific Software), http://www.certif.com.

Zakri, C., Renault, A., Rieu, J., Vallade, M., Berge, B., Legrand, J., Vignault, G. & Grübel, G. (1997). *Phys. Rev. B*, **55**, 14163–14172.